



# CHORUS

This is the accepted manuscript made available via CHORUS. The article has been published as:

## Orbital mapping of energy bands and the truncated spin polarization in three-dimensional Rashba semiconductors

Qihang Liu, Xiuwen Zhang, J. A. Waugh, D. S. Dessau, and Alex Zunger

Phys. Rev. B **94**, 125207 — Published 27 September 2016

DOI: [10.1103/PhysRevB.94.125207](https://doi.org/10.1103/PhysRevB.94.125207)

# Orbital mapping of energy bands and the truncated spin polarization in three-dimensional Rashba semiconductors

Qihang Liu<sup>1,\*</sup>, Xiuwen Zhang<sup>1</sup>, J. A. Waugh<sup>2</sup>, D. S. Dessau<sup>1,2</sup> and Alex Zunger<sup>1</sup>

<sup>1</sup>University of Colorado, Boulder, Renewable and Sustainable Energy Institute Colorado 80309, USA

<sup>2</sup>Department of Physics, University of Colorado, Boulder, Colorado 80309, USA

\*Email: [qihang.liu85@gmail.com](mailto:qihang.liu85@gmail.com).

PACS: 71.70.Ej, 75.70.Tj, 75.10.Dg

## Abstract

Associated with spin-orbit coupling (SOC) and inversion symmetry breaking, Rashba spin polarization opens a new avenue for spintronic applications that was previously limited to ordinary magnets. However, spin polarization effects in actual Rashba systems are far more complicated than what conventional single-orbital models would suggest. By studying via first-principles DFT and a multi-orbital  $k \cdot p$  model a 3D bulk Rashba system (free of complications by surface effects) BiTeI, we find that the physical origin of the leading spin polarization effects is SOC-induced hybridization between spin *and multiple orbitals*, especially those with nonzero orbital angular momenta. In this framework we establish a general understanding of the orbital mapping, common to the surface of topological insulators and Rashba system. Consequently, the intrinsic mechanism of various spin polarization effects, which pertain to all Rashba systems even those with global inversion symmetry, is understood as a manifestation of the orbital textures. This finding suggests a route for designing high spin-polarization materials by considering the atomic-orbital content.

## I. Introduction

The coupling between the motion of electrons and spins leading to spin polarization without external magnetic field is the focus of the emerging field of spin-orbitronics<sup>1,2</sup>, a branch of spintronics<sup>3</sup> that encompasses many interesting areas such as the Dresselhaus<sup>4</sup> and the Rashba<sup>5</sup> effects, spin-orbital torque<sup>6,7</sup>, topological insulation<sup>8</sup>, and Majorana fermions<sup>9</sup>. The idea of control of spin degree of freedom even without external magnetic field is based on the fact that in a non-centrosymmetric system, spin-orbit coupling (SOC) sets up an effective internal magnetic field that creates spin splitting  $E_1(\mathbf{k}, \uparrow) - E_2(\mathbf{k}, \downarrow)$  between spin-up and spin-down components in bands 1 and 2 away from the time-reversal invariant wavevector  $K^*$ . Specifically, Rashba spin splitting provides a classical scenario of spin topology encoded already in a simplified *single-orbital* (e.g., one  $s$  band) Hamiltonian  $H = \hbar^2 \mathbf{k}^2 / 2m^* + \lambda (\nabla V \times \mathbf{k}) \cdot \boldsymbol{\sigma}$ , where fully spin-polarized bands form two oppositely rotating spin loops at Fermi surface. However, the limitation of the single-orbital model is already acknowledged in areas of condensed matter physics, such as strongly correlated systems<sup>10</sup>. In real materials with spin coupling to *multiple* orbitals that make up the band eigenstates, the leading SOC spin effects that deviate from the classical single-orbital picture include: (i) the spin polarization  $S_n(\mathbf{k})$  of each spin-split band ( $n, \mathbf{k}$ ) appears to be truncated below its maximum value 100%; (ii) Each branch of the pair of spin-split bands (that are degenerate without SOC) experiences different degrees of spin truncation away from the time-reversal invariant wavevector  $K^*$ , resulting in a net *spin polarization* for the band pair (iii) The Rashba bands with two loops of energy contours can have identical helicities of spin texture. These effects were studied primarily in two-dimensional (2D) metallic surfaces — the classic Rashba systems<sup>11-17</sup>. Effect (i) and (ii) were theoretically discussed for freestanding Au(111) films<sup>11</sup>, and in BiAg<sub>2</sub> metallic surface alloys<sup>12, 17</sup>, while effect (iii) was predicted in the unoccupied bands of Bi/Cu(111)<sup>13</sup> and Bi/Ag(111)<sup>15</sup> surface alloys. The physics behind these intriguing spin effects was briefly touched upon in the context of 2D Rashba metallic films as being a consequence of the coupling between spin and different in-plane orbitals<sup>13, 17</sup>. However, in all 2D Rashba platform noted above there is a need for a free surface to observe the effects, so ordinary surface effects (such as broken bonds and surface band

bending<sup>18</sup>) can cloud the intrinsic mechanism of these spin effects to be well established<sup>14</sup>.

By extending the spin effects (i)-(iii) from the originally studied 2D metallic Rashba systems to 3D surface-free bulk Rashba semiconductors, we provide two pertinent generalizations: (a) We use the construct of *orbital texture* [a  $k$ -space map  $I_n^{(l,m)}(k_x, k_y)$  of the content of orbital  $m_l$  in band  $n$ , see Eq. (1)] familiar from topological insulators<sup>19-23</sup>. We point out that the effect of switch in orbital texture between two bands is common to topological insulators and to 3D Rashba semiconductors. Specifically, in the topologically-trivial bulk Rashba semiconductor the orbital textures of different Rashba bands switches from “radial” to “tangential” (with respect to the energy contour) character at the band crossing wavevector  $K^*$ , in full analogy with the phenomena previously observed<sup>20,23,24</sup> and calculated<sup>22,23</sup> at the *surfaces* of 3D topological insulator (TI) Bi<sub>2</sub>Se<sub>3</sub>. Thus, the switch of orbital texture and indeed effects (i)-(iii) are not specific to topological or Rashba effects, but originate fundamentally from the fact that energy bands in complex solids invariably show a mixture of different azimuthal total orbital angular momentum (OAM)  $m_j$ , and that SOC can induce hybridization specifically between spin and *multiple* orbitals especially those with nonzero  $m_l$ , respectively. (b) We show that the spin polarization truncated by multiple orbital hybridization can be generalized even to systems with global inversion symmetry, manifesting the “hidden spin polarization effect”<sup>25</sup>. The understanding of effects (i)-(iii) and their reflection in the switch in orbital texture could provide better design guidelines for material selection and for spin manipulation in actual material application, e.g., electron confinement induced by spin-flip backscattering<sup>17</sup> and spin-galvanic effect<sup>26,27</sup>.

We reached these conclusions by applying density functional theory (DFT) and a multi-band  $k \cdot p$  model to a 3D bulk Rashba compound BiTeI<sup>28</sup>. We find that within the six energy bands near the Fermi level ( $E_F$ ) there are (i) large spin truncation per band at the band crossing wavevector  $K^*$  with the residual spin polarization ranging from 0% to 85% far greater than the ~5 % seen in Au [111] surface; (ii) a net *spin polarization of band pairs* up to 50% for the top two valence bands, and (iii) identical spin-rotating loops at the occupied bands that can be examined by future angle-resolved photon emission spectroscopy (ARPES) measurements.

## II. Methods

We use the density functional theory (DFT) with the projector-augmented wave (PAW) pseudopotential<sup>29</sup> and the generalized gradient approximation to exchange and correlation of Perdew, Burke and Ernzerhof (PBE)<sup>30</sup>. The plane wave basis set size reflected in energy cutoff is 500 eV, and the total energy minimization was performed with a tolerance of  $10^{-5}$  eV. Spin-orbit coupling is calculated self-consistently by a perturbation  $\sum_{i,l,m} V_l^{SO} \vec{L} \cdot \vec{S} |l, m, i\rangle \langle l, m, i|$  to the pseudopotential<sup>31</sup>, where  $|l, m, i\rangle$  is the angular momentum eigenstate of  $i$ -th atomic site. The orbital intensity and orbital-dependent spin polarization is calculated by projecting the wave functions  $\psi_n(\mathbf{k})$  with plane-wave expansion on the orbital basis (spherical harmonics) of each atomic site, as written in the following:

$$\text{Orbital intensity: } I_n^{(l,m)}(\mathbf{k}) = \langle \psi_n(\mathbf{k}) | (|l, m, i\rangle \langle l, m, i|) | \psi_n(\mathbf{k}) \rangle. \quad (1)$$

$$\text{Orbital-dependent spin polarization: } S_n^{(i,l,m)}(\mathbf{k}) = \langle \psi_n(\mathbf{k}) | (\boldsymbol{\sigma} \otimes |l, m, i\rangle \langle l, m, i|) | \psi_n(\mathbf{k}) \rangle. \quad (2)$$

Where  $n$ ,  $\mathbf{k}$  and  $\boldsymbol{\sigma}$  denote band index, momentum and Pauli matrix, respectively. Note that in this study we only distinguish different  $|l, m\rangle$  states by adding up all the sites. All these features are implemented in the Vienna ab initio package (VASP)<sup>32</sup>.

## III. Truncated spin polarization, net spin polarization and spin texture in BiTeI

This compound is a 3D bulk semiconductor [space group  $P3m1$ , see Fig. 1(a)] that manifest strong SOC, the ensuing orbital hybridization, and a polar field due to the positively charged Bi-Te layer that connects to the negatively charged iodine layer. The consequent Rashba spin-split bands<sup>28,33</sup> from DFT calculations are shown in Fig. 1(b). We focus on the top four hole bands VB1-VB4 (going down from  $E_F$ ) and bottom two electron bands CB1-CB2 (going up from  $E_F$ ) around the  $K^* = A(0,0,0.5)$  wavevector. The spin polarization  $S_n(\mathbf{k})$  ( $n = \text{VB1-VB4, CB1-CB2}$ ) along  $k_y$  direction is shown in Fig. 1(c). In what follows we discuss spin effects (i)-(iii) in bulk BiTeI:

(i) *Truncation of single band spin polarization*: The band-by-band spin polarization is calculated as the expectation value of the spin operator in each of the six spin-split bands at the wavevector  $K^*$ . We find that the magnitude of spin polarization is below the

maximal magnitude of 100%. For VB1, VB2 and CB1, CB2 the spin polarization is  $\pm 85\%$  and  $\pm 51\%$ , respectively, while for VB3, VB4 the spin polarization is 0, i.e., a complete quenching of spin. Away from the band crossing wavevector  $K^*$  the spin polarization of VB1 and VB2 evolves quite differently with  $k_y$ . VB1 is highly spin polarized in the considered momentum range up to  $S_{VB1} = -96\%$ . while VB2 loses its spin polarization rapidly with increasing  $k_y$  down to  $S_{VB2} = 46\%$ .

(ii) *Net spin polarization of pairs of spin-split bands*: If we sum  $S_{VB1}(\mathbf{k})$  and  $S_{VB2}(\mathbf{k})$  (which would add up to zero in the absence of SOC), we find a *net* spin up of  $-50\%$  at  $k_y = 0.06 \text{ \AA}^{-1}$ . On the other hand, the sum of  $S_{VB3}(\mathbf{k})$  and  $S_{VB4}(\mathbf{k})$  reaches  $48\%$  at  $k = 0.06 \text{ \AA}^{-1}$ , while  $S_{CB1}(\mathbf{k})$  and  $S_{CB2}(\mathbf{k})$  change slightly with  $k$ . We note that the position of the net polarization peak does not overlap with the energy peak in the band structure which locates at  $k = 0.09 \text{ \AA}^{-1}$  in  $k_y$  direction, suggesting that the spin polarization is not a reflection of the eigenvalue dispersion.

(iii) *Identical directions of spin-rotation in the helical spin texture bands*: The band pair VB1+VB2 and the pair CB1+CB2 show the classical Rashba-type spin texture, i.e., opposite helicities of spin loops. However, as shown in Fig. 1(c) before  $S_{VB4}$  falls below 0,  $S_{VB3}$  and  $S_{VB4}$  have the same sign, implying two spin loops with the same helicity in the area of  $|k_{//}| < 0.10 \text{ \AA}^{-1}$ .

All three spin effects discussed above are absent in the conventional single-orbital model and thus reflect a manner of the complex interplay between spin and various OAM under the regime of SOC. To get a full picture it is useful to consider the *orbital texture*, i.e., the  $k$ -space map  $I_n^{(l,m)}(k_x, k_y)$  of the content of orbital  $m_l$  in band  $n$ .

#### IV. Orbital texture and its behavior for different bands

In real solids the orbital content generally varies with the wavevector and band index, reflecting the changing symmetry. The orbital intensity is obtained by projecting the SOC-relevant band eigenstate  $(n, \mathbf{k})$  onto local orbitals on atomic sites as shown in Eq. (1). Figures 2(a)-2(d) show the DFT calculated orbital texture given by  $p_y$  orbital intensity at different energy contours relative to  $K^*$ , for VB1 and VB2. We find that for VB1 the calculated  $p_y$  orbital texture component is maximal along the  $k_y$  direction and

minimal along  $k_x$  (where the  $p_x$  orbital dominates the in-plane states). On the other hand, for VB2 the  $p_y$  orbital texture component is minimal along  $k_y$  and maximal along  $k_x$ . Thus, the orbital texture of VB1 and VB2 are different from each other and dominated, by *radial* and *tangential* in-plane orbital patterns, respectively. This difference leads to a radial-tangential orbital texture *switch*. To trace the switch between these two bands we follow Ref. <sup>23</sup> to define the in-plane orbital polarization  $\lambda$  as a function of momentum  $k$  and band index  $n$  as  $\lambda(n, \mathbf{k}) = \frac{I(p_x) - I(p_y)}{I(p_x) + I(p_y)}$ , where  $I(p_{x,y})$  denotes the calculated orbital intensity of  $p_{x,y}$ . Figure 2e shows  $\lambda$  as a function of the in-plane azimuth angle  $\theta$  (defined in Fig. 2b), confirming the switch of the intensity distribution in going from VB1 to VB2. Moreover, the intensity variation fits very well to a  $\sin 2\theta$  or  $\cos 2\theta$  distribution, with a period of  $\pi$ . As shown in Fig. 2f,  $\lambda$  changes the sign as the momentum  $k_y$ , passing through  $K^*$ , indicating that the radial-tangential switch happens exactly at the band crossing wavevector. For VB3 and VB4 the orbital textures also have a switch between tangential and radial characters at  $K^*$  (see Fig. 3a and b). On the other hand, in CB1 and CB2 both Bi and Te atoms have considerable  $p_{x,y}$  components, but with different orbital textures. For  $p_{x,y}$  orbitals of Bi atom there is a radial-tangential switch from CB1 to CB2, while for  $p_{x,y}$  orbitals of Te atom the orbital switch has an opposite trend, i.e., tangential-radial (see Fig. 3c-f). This observation agrees closely with the recent ARPES measurement by King et al. on the conduction surface state of BiTeI <sup>34</sup>, and further confirms that such intriguing behavior comes from the intrinsic bulk state rather than any surface effects.

## V. Universality of orbital texture in bulk Rashba and surface of TI revealed by $\mathbf{k} \cdot \mathbf{p}$ modeling

The orbital texture switch between two bands at  $K^*$  in the topologically-trivial semiconductor bares an interesting analogy to the recently observed angle-resolved photon emission spectroscopy (ARPES) measurements <sup>20, 23</sup> and DFT calculations <sup>22</sup> at the *surfaces* of TI Bi<sub>2</sub>Se<sub>3</sub>. Here we use a *multi-orbital*  $\mathbf{k} \cdot \mathbf{p}$  model to illustrate how mixing orbitals of different  $m_l$  and  $m_j$  couple with spin and lead to the orbital texture switch and the spin polarization effects (i)-(iii). The crucial basis set represented in terms of  $m_j$  is obtained in DFT; we now explicitly isolate it from all other DFT bands in  $\mathbf{k} \cdot \mathbf{p}$  model below. Taking VB1 and VB2 as an example, we consider the SOC Hamiltonian as

a perturbative form  $H_R = \alpha(\sigma_y k_x - \sigma_x k_y)$  that is valid for both Rashba bulk and TI surface<sup>22</sup>, and thus write the wavefunctions in the vicinity of  $K^*$  as:

$$|VB1, k\rangle = \frac{1}{\sqrt{2}}(\sqrt{1 - \omega_{VB}^2} + \mu_{VB}k)|p_t\rangle \otimes |LH\rangle + \left[\frac{i}{\sqrt{2}}(-\sqrt{1 - \omega_{VB}^2} + \nu_{VB}k)|p_r\rangle + (\omega_{VB} - \xi_{VB}k)|Z\rangle\right] \otimes |RH\rangle \quad (3)$$

$$|VB2, k\rangle = \frac{1}{\sqrt{2}}(-\sqrt{1 - \omega_{VB}^2} + \mu_{VB}k)|p_t\rangle \otimes |RH\rangle + \left[\frac{i}{\sqrt{2}}(\sqrt{1 - \omega_{VB}^2} + \nu_{VB}k)|p_r\rangle + (\omega_{VB} + \xi_{VB}k)|Z\rangle\right] \otimes |LH\rangle \quad (4)$$

Where the in-plane  $p$  orbital basis are tangential  $|p_t\rangle = -\sin\theta|p_x\rangle + \cos\theta|p_y\rangle$  and radial  $|p_r\rangle = \cos\theta|p_x\rangle + \sin\theta|p_y\rangle$ ;  $|Z\rangle = \omega_s|s\rangle + \omega_z|p_z\rangle$  with  $|\omega_s|^2 + |\omega_z|^2 = 1$ ; the spin basis are eigenstates of  $H_R$ , i.e., LH and RH helical spin states  $|LH\rangle = \frac{1}{\sqrt{2}}\begin{pmatrix} ie^{-i\theta} \\ 1 \end{pmatrix}$  and  $|RH\rangle = \frac{1}{\sqrt{2}}\begin{pmatrix} -ie^{-i\theta} \\ 1 \end{pmatrix}$ ; and  $\omega_{VB}$ ,  $\nu_{VB}$ ,  $\xi_{VB}$  are the wavefunction coefficients that are band-dependent. More details on these wavefunctions can be found in Appendix. By calculating the difference of  $p_t$  and  $p_r$  intensity and omitting the higher-order  $k$  term we find that

$$[Int(p_t) - Int(p_r)]|_{VB1(VB2)} = \pm|k|[\sqrt{1 - \omega_{VB}^2}(\mu_{VB}^* - \nu_{VB}^*) + c. c.] \quad (5)$$

From the modeling wavefunctions Eq. (3) and (4) and the difference of  $p_t$  and  $p_r$  intensity shown in Eq. (5), clear evidence is provided that the dominant in-plane orbital is different for the two spin-split valence bands, in other words the radial-tangential *orbital texture switches* at  $k = 0$ , i.e., the band crossing point  $K^*$ . The model also reveals that the symmetry lowering away from  $K^*$  permits the mixing of new  $m_j = \pm 3/2$  ( $|+\rangle \otimes |\uparrow\rangle$  and  $|-\rangle \otimes |\downarrow\rangle$ , or “heavy hole” like) components into the  $K^*$  wavefunctions ( $m_j = \pm 1/2$  for the VB1 and VB2 of BiTeI), leading to the orbital texture switch.

Benefiting from the truncated basis set represented in terms of  $m_j$ , as distilled from the all-orbital DFT representation, we conclude that the underlying physical origin of the common behavior in both TI and non-TI materials is the SOC symmetry-enforced hybridization of different azimuthal total OAM  $m_j$  components into band eigenstates. This hybridization was absent at the high symmetry  $K^*$  point. Thus, this effect is not

limited to topological insulators but is far more general and applies also to Rashba compounds that are topological-trivial bulk semiconductors such as BiTeI<sup>34</sup>. It is noticeable that the orbital switch is generally a small  $k$  effect available only in the vicinity of  $K^*$ , where  $p_x$  and  $p_y$  orbitals have equal intensity. Comparing with TI surface states, the Hamiltonian of BiTeI has an additional kinetic term  $\hbar^2 k^2 / 2m^*$ , leading to two parabolic-like branches with a critical band crossing point. Unlike the TI Dirac cone, the band crossing point in a Rashba semiconductor seems trivial, but it still manifests such orbital texture switch, indicating the physical origin from the fundamental spin-orbital effects rather than the topological feature.

From Eq. (5) we can see that the orbital switch for both TI surface and Rashba bulk must occur at a critical point (Dirac point in TI and band crossing point in Rashba semiconductor) because of the symmetric form of the wavefunctions. However, the question of which orbital dominates a certain state depends on the wavefunction coefficients, which is *material-dependent*. Therefore, if the sample is inverted within a fixed laboratory frame (like the bottom surface of TI), the orbital texture will remain unchanged. On the other hand, the chirality of the spin texture of the Rashba system is *coordinate-dependent*. The helical spin texture will change the chirality by the inversion of sample, due to the flip of the polar field inside the crystal. This is analogous to the top and bottom surface states of Bi<sub>2</sub>Se<sub>3</sub> in which the spin texture is opposite but the orbital texture has the same switching trend. We can also expect the truncated spin polarization and uncompensated spin polarization at the same  $k$  point for upper and lower Dirac cone<sup>24, 35-38</sup> from the discussion mentioned above.

## VI. Understanding the spin polarization effects

Eq. (3) and (4) show that each orbital component couples with a certain spin state, forming *orbital-dependent spin textures* [see Eq. (2)]. Maximal spin magnitude arises when every orbital-dependent spin texture co-aligns, i.e., has the same helicity. This requires that the band eigenstate be composed exclusively of orbitals with the same azimuthal quantum number  $m_l$ . In real materials where SOC mixes orbitals with different  $m_l$  in one eigenstate  $(n, \mathbf{k})$ , the corresponding spin polarization is truncated relative to its maximal value. Specifically, the tangential in-plane orbital ( $p_t$ ) always couples opposite

spin texture to that of radial in-plane orbital ( $p_r$ ),  $s$  and  $p_z$  orbital. At the wavevector  $A$  with  $k \rightarrow 0$ ,  $p_t$  and  $p_r$  components have the same intensity but opposite spin pattern and thus cancel each other, making the spin polarization  $S(k \rightarrow 0) = |\omega_{VB}|^2$  all contributed by  $s$  and  $p_z$  orbital. This scenario gives the truncated spin polarization at  $K^*$  for all the bands shown in Fig. 1c. The total spin polarization summing over all bands is equivalent to the value obtained from the contributions of  $m_l = 0$  states, e.g.,  $s$ ,  $p_z$ , and  $d_z^2$ , etc. This statement is valid also in the traditional 2D Rashba systems like Au(111) surface<sup>11</sup>, in which the surface Rashba bands are nearly exclusively composed by the  $s$  and  $p_z$  states, and thus have nearly 100% spin polarization.

Due to the orbital texture switch, we find from Eq. (3) and (4) that the dominate in-plane  $p$  orbitals of a pair of Rashba bands couple to spin textures with the same helicity. This fact is confirmed by DFT calculation showing that the dominating radial orbital for VB1 and tangential orbital for VB2 both have RH spin texture (see Fig. 4). In BiTeI, the wavefunctions of VB1 and VB2 are dominated by  $s+p_z$  orbitals [Te- $p_z$  (~50%), I- $p_z$  (~13%) and Bi- $s$  (13%)]. We consider here two categories of orbitals classified by  $m_l = 0$  ( $s$  and  $p_z$  for all sites) and  $m_l \neq 0$  (in-plane  $p_x$  and  $p_y$  for all sites) and examine the corresponding spin textures coupled by these two classes. The  $s+p_z$ -dependent spin texture has opposite helicity for VB1 and VB2, i.e., VB1 has a right-handed (RH) spin texture, while VB2 has a left-handed (LH) spin texture (see Fig. 5). On the other hand, the in-plane orbital ( $p_x+p_y$ ) also contributes helical spin textures, but these orbital-dependent spin textures have the same RH helicity for both VB1 and VB2, as shown in the white arrows in Fig. 4a and b. This can also be understood by multi-orbital model Eq. (1) and (2), where the  $p_r$  ( $p_t$ ) orbitals always provide positive (negative) contributions to the  $s+p_z$ -orbital dependent spin textures. Consequently, at a finite  $k$  the different intensity of  $p_t$  and  $p_r$  orbitals for VB1 and VB2 can cause different spin magnitudes to the respective bands, and thus a nonzero net spin polarization  $S_1(k) + S_2(k)$ . From Fig. 4a we find that for VB1  $p_r$  dominates the in-plane orbital, so the in-plane spin texture followed the radial feature, i.e., RH. On the other hand, for VB2  $p_t$  dominates the in-plane orbital as shown in Fig. 4b, so the total in-plane spin texture is still RH. Therefore, by summing the in-plane orbital contribution and the  $s+p_z$  orbital contribution to the spin textures, the

total spin polarization shows different spin truncation for VB1 and VB2, as shown in Fig. 1(c).

Similar to VB1 and VB2, the degenerate state at A in CB1 and CB2 are also  $m_j = \pm 1/2$  states. Therefore, they have the form of wave functions analogous to Eq. (3) and (4), but with different wavefunction coefficients. DFT shows that the weight of the  $s+p_z$  orbital and in-plane  $p$  orbital is about 50%:50% at A [Bi- $p_z$  (~35%), Te- $p_{x,y}$  (~27%) and Bi- $p_{x,y}$  (18%)], leading to  $\pm 0.5$  spin polarization. The spin textures as well as the  $p_{x,y}$  and  $s+p_z$  orbital-dependent spin textures for CB1 and CB2 is shown in Fig. 6. We find that the total spin texture is predominately contributed by  $p_z$  orbital, while the  $p_{x,y}$  orbital-dependent spin texture is negligible. This is because of the competition between the  $p_{x,y}$  orbital textures of Bi and Te atom. Recalling that the tangential and radial orbitals always couple opposite spin textures [see Eq. (3) and (4)], the similar distribution of the two kinds of orbitals in each conduction band leads to a cancelling of in-plane orbital-dependent spin texture (see Fig. 3). In contrast, VB1 and VB2 have less  $p_{x,y}$  components and are mainly from a single source (Te atom), so they manifest a larger spin magnitude and non-compensation effect by the same helicity of the in-plane orbital-dependent spin textures.

For VB3 and VB4,  $p_t$  and  $p_r$  dominate the whole state around  $K^*$ , respectively. Therefore, VB3 and VB4 bands are  $m_j = \pm 3/2$  states with the corresponding wavefunctions at  $K^*$  containing only in-plane  $p$  components:  $|p_+\rangle \otimes |\uparrow\rangle$  and  $|p_-\rangle \otimes |\downarrow\rangle$ , leading to the complete quenching of spin. Consequently, the total spin textures form two LH helical spin loops (see Fig. 3). Unlike the case in Bi/Cu(111)<sup>13</sup> and Bi/Ag(111)<sup>15</sup> surface alloys, these identical spin-rotating loops occur at the occupied bands that is detectable by ARPES measurements.

## VII. Effects of different SOC strength

To demonstrate that the intriguing spin polarization effects originate from SOC we artificially rescaled the strength of SOC with adding a multiplier  $\Delta$  on the SOC Hamiltonian ( $\Delta = 1$  for the real system). The spin magnitude and spin splitting energy  $E_R$  for VB1 and VB2 of BiTeI as a function of  $\Delta$  is shown in Fig. 7. Using a small SOC strength  $\Delta = 0.01$  and extrapolate the results to  $\Delta = 0$ , we find that the two valence bands

are degenerated with fully polarized spin-up and spin-down component [ $S_1(k_1) = -1$  and  $S_2(k_1) = 1$ ] with the absence of SOC. At this time the A states are composed by pure  $m_l = 0$  orbitals, i.e.,  $s$  and  $p_z$ . When increasing  $\Delta$ , there is a reduction on spin magnitude at  $k_1 \rightarrow 0$ , i.e., the A point, due to the mixture of in-plane p orbitals. On the other hand, the spin polarizations of VB1 and VB2 apparently compensate with each other at A with  $S_1(k_1) + S_2(k_1) = 0$ , while away from the A point such as  $k_2 = 0.06 \text{ \AA}^{-1}$ , the sum of spin magnitude of the valence bands deviates from zero with the increasing  $\Delta$ . Therefore, it clearly shows that SOC not only manifests an energy splitting between spin polarized bands, but also introduces a complex interplay between spin and multi-orbitals leading to various spin polarizations effects.

### VIII. Generalizing to systems with inversion symmetry

The truncated spin polarization and the net polarization effect are illustrated above in a Rashba semiconductor BiTeI. However, we are not using any special feature of this orbitally-hybridized compound other than SOC-induced (Rashba) spin splitting, and thus expect our finding to pertain to a very broad range of such compounds, whether inversion symmetry is present or not. In centrosymmetric crystals the spin bands are degenerate in  $E$  vs  $k$  momentum space, but this does not mean that the spins are mixed in position space. Correspondingly, the centrosymmetric systems with lower-symmetry sectors could manifest a “hidden” form of spin polarization named R-2 effect<sup>25, 39</sup>. Like two oppositely stacked Rashba layers, in R-2 system there is still finite spin polarization localized on each atomic site  $i$  that feels inversion-asymmetric environment, and such polarization is compensated in  $k$  space by another atom forming inversion partner of site  $i$ . Therefore, if we consider the local spin polarization in real space, i.e., localized on one inversion-asymmetric atoms or sectors, the spin truncation effects also happen when spin is coupled by multi-orbitals with different  $m_l$ . It is noticeable that the orbital-dependent spin texture is robust against small perturbation that breaks the global inversion symmetry such as electric fields, which is highly feasible for the detection on experiments.

We choose a centrosymmetric R-2 material LaOBiS<sub>2</sub> (using the reported space group  $P4/nmm$ ) to illustrate the truncation effects. Figure 8(a) and (e) exhibits the projected atomic-orbital dependent spin textures of LaOBiS<sub>2</sub> on one BiS<sub>2</sub> layer of the two-fold

degenerated conduction band minimum (CBM) and valence band maximum (VBM), respectively. The local spin textures on the other BiS<sub>2</sub> layer is exactly opposite formed<sup>25</sup>, and not shown here. All the spin textures are in the  $x$ - $y$  plane, with almost zero  $z$ -component. We observe helical spin for holes but non-helical spin for electrons, suggesting Rashba-type polarization (R-2) and the combination of Rashba and Dresselhaus effects (R-2 and D-2) for VBM and CBM, respectively. In general, the environment of R-2 material contains simultaneously polar field and inversion asymmetry, indicating the coexistence of R-2 and D-2 effects, depending on different band characters.

We note that the hole spin is nearly fully polarized with the spin magnitude  $\sim 90\%$ , while the electron spin is only  $\sim 30\%$  polarized. Besides the spin mixture effect due to the interlayer coupling (vanished along  $X$ - $M$  direction), the reason that leads to the partially polarization is the diverse atomic-orbital dependent spin textures. Figure 8b-d and 8f-h shows the spin textures from different atomic orbitals within one BiS<sub>2</sub> layer. We see all the orbital-dependent spin textures are parallel or antiparallel to the total spin texture, and they can make either positive or negative effects on the total spin polarization. We consider 4 atomic orbitals  $s$ ,  $p_x$ ,  $p_y$ , and  $p_z$  for each site of one BiS<sub>2</sub> layer. Table I shows the sign of spin polarization induced by each atomic orbital of different sites, valid for both VB and CB. The whole expectation of the local spin is calculated by adding all the 12 orbital-projected components. Looking into different orbitals, we find that for each site,  $s$ ,  $p_x$ , and  $p_z$  has the same spin direction, while  $p_y$  always has opposite one, which is determined by the band symmetry character around  $X$  point. At the  $X$  (0, 1/2, 0) point, the nonequivalence between  $x$  and  $y$  direction leads to anisotropic feature between  $p_x$  and  $p_y$ . The VBM is mainly composed of Bi- $s$  and S- $p_y$  states, with the same spin helicity (2 “+”). On the other hand, the CBM is dominated by Bi- $p_x$  and  $p_y$  states, which couple antiparallel spin textures (1 “+” and 1 “-”). Therefore, the total spin polarization of electrons is strongly reduced comparing with the holes.

## IX. Discussion and design implications

In the past few years wide areas of physics and material science that related to SOC build up the new field spin-orbitronics. By generalizing the previously observed orbital

texture switch in TI surface to a bulk Rashba semiconductor, we unveil the deeper mechanism of various spin polarization effects that is unexpected in the simple Rashba model, and provide a clear picture of the delicate interplay between spin and multi-orbitals. Our work is also expected to open a route for designing by the atomic-orbital feature high spin-polarization materials that are of vital importance for nonmagnetic spintronic applications<sup>3</sup>. For example, in Rashba splitting the in-plane spin drives a current perpendicular to the direction of spin polarization induced by the asymmetric Elliot-Yafet spin-relaxation, named spin-galvanic effect<sup>26, 27</sup>. Since the current is proportional to the average magnitude of the spin polarization, the effects of spin truncation and that different branches experience different degrees of spin polarization could have a more complex impact on the conversion process between spin and current in a Rashba system, which calls for further investigation.

## Acknowledgement

We are grateful for helpful discussions with Dr. Yue Cao. This work was supported by NSF Grant No. DMREF-13-34170. This work used the Extreme Science and Engineering Discovery Environment (XSEDE), which is supported by National Science Foundation grant number ACI-1053575.

## References

1. Manchon, A.; Koo, H. C.; Nitta, J.; Frolov, S. M.; Duine, R. A. *Nat Mater* **2015**, 14, (9), 871-882.
2. Ciccarelli, C.; HalsKjetil, M. D.; Irvine, A.; Novak, V.; Tserkovnyak, Y.; Kurebayashi, H.; Brataas, A.; Ferguson, A. *Nat Nano* **2015**, 10, (1), 50-54.
3. Žutić, I.; Fabian, J.; Das Sarma, S. *Reviews of Modern Physics* **2004**, 76, (2), 323-410.
4. Dresselhaus, G. *Phy. Rev.* **1955**, 100, (2), 580-586.
5. Bychkov, Y. A.; Rashba, E. I. *Soviet Journal of Experimental and Theoretical Physics Letters* **1984**, 39, 78.
6. Manchon, A. *Nat Phys* **2014**, 10, (5), 340-341.
7. KurebayashiH; Sinova, J.; FangD; Irvine, A. C.; Skinner, T. D.; WunderlichJ; NovakV; Campion, R. P.; Gallagher, B. L.; Vehstedt, E. K.; Zarbo, L. P.; VybornyK; Ferguson, A. J.; JungwirthT. *Nat Nano* **2014**, 9, (3), 211-217.
8. Hasan, M. Z.; Kane, C. L. *Reviews of Modern Physics* **2010**, 82, (4), 3045-3067.

9. Mourik, V.; Zuo, K.; Frolov, S. M.; Plissard, S. R.; Bakkers, E. P. A. M.; Kouwenhoven, L. P. *Science* **2012**, 336, (6084), 1003-1007.
10. Koga, A.; Kawakami, N.; Rice, T. M.; Sigrist, M. *Physical Review Letters* **2004**, 92, (21), 216402.
11. Henk, J.; Ernst, A.; Bruno, P. *Physical Review B* **2003**, 68, (16), 165416.
12. Bihlmayer, G.; Blügel, S.; Chulkov, E. V. *Physical Review B* **2007**, 75, (19), 195414.
13. Mirhosseini, H.; Henk, J.; Ernst, A.; Ostanin, S.; Chiang, C. T.; Yu, P.; Winkelmann, A.; Kirschner, J. *Physical Review B* **2009**, 79, (24), 245428.
14. Hirayama, H.; Aoki, Y.; Kato, C. *Physical Review Letters* **2011**, 107, (2), 027204.
15. Wissing, S. N. P.; Schmidt, A. B.; Mirhosseini, H.; Henk, J.; Ast, C. R.; Donath, M. *Physical Review Letters* **2014**, 113, (11), 116402.
16. Krasovskii, E. E. *Journal of Physics: Condensed Matter* **2015**, 27, (49), 493001.
17. Schirone, S.; Krasovskii, E. E.; Bihlmayer, G.; Piquerel, R.; Gambardella, P.; Mugarza, A. *Physical Review Letters* **2015**, 114, (16), 166801.
18. Bahramy, M. S.; King, P. D. C.; de la Torre, A.; Chang, J.; Shi, M.; Patthey, L.; Balakrishnan, G.; Hofmann, P.; Arita, R.; Nagaosa, N.; Baumberger, F. *Nat. Commun.* **2012**, 3, 1159.
19. Zeljkovic, I.; Okada, Y.; Huang, C.-Y.; Sankar, R.; Walkup, D.; Zhou, W.; Serbyn, M.; Chou, F.; Tsai, W.-F.; Lin, H.; Bansil, A.; Fu, L.; Hasan, M. Z.; Madhavan, V. *Nat Phys* **2014**, 10, (8), 572-577.
20. Xie, Z.; He, S.; Chen, C.; Feng, Y.; Yi, H.; Liang, A.; Zhao, L.; Mou, D.; He, J.; Peng, Y.; Liu, X.; Liu, Y.; Liu, G.; Dong, X.; Yu, L.; Zhang, J.; Zhang, S.; Wang, Z.; Zhang, F.; Yang, F.; Peng, Q.; Wang, X.; Chen, C.; Xu, Z.; Zhou, X. *Nat Commun* **2014**, 5, 3382.
21. Zhiyong, Z.; Yingchun, C.; Udo, S. *New Journal of Physics* **2013**, 15, (2), 023010.
22. Zhang, H.; Liu, C.-X.; Zhang, S.-C. *Physical Review Letters* **2013**, 111, (6), 066801.
23. Cao, Y.; Waugh, J. A.; Zhang, X. W.; Luo, J. W.; Wang, Q.; Reber, T. J.; Mo, S. K.; Xu, Z.; Yang, A.; Schneeloch, J.; Gu, G. D.; Brahlek, M.; Bansal, N.; Oh, S.; Zunger, A.; Dessau, D. *S. Nat Phys* **2013**, 9, (8), 499-504.
24. Zhu, Z. H.; Veenstra, C. N.; Levy, G.; Ubaldini, A.; Syers, P.; Butch, N. P.; Paglione, J.; Haverkort, M. W.; Elfimov, I. S.; Damascelli, A. *Phys. Rev. Lett.* **2013**, 110, (21), 216401.
25. Zhang, X.; Liu, Q.; Luo, J.-W.; Freeman, A. J.; Zunger, A. *Nat. Phys.* **2014**, 10, 387-393.
26. Ganiehev, S. D.; Schneider, P.; Bel'kov, V. V.; Ivchenko, E. L.; Tarasenko, S. A.; Wegscheider, W.; Weiss, D.; Schuh, D.; Mordin, B. N.; Phillips, P. J.; Pidgeon, C. R.; Clarke, D. G.; Merrick, M.; Murzyn, P.; Bregulin, E. V.; Prettl, W. *Physical Review B* **2003**, 68, (8), 081302.
27. Ganiehev, S. D.; Ivchenko, E. L.; Bel'kov, V. V.; Tarasenko, S. A.; Sollinger, M.; Weiss, D.; Wegscheider, W.; Prettl, W. *Nature* **2002**, 417, (6885), 153-156.
28. Ishizaka, K.; Bahramy, M. S.; Murakawa, H.; Sakano, M.; Shimojima, T.; Sonobe, T.; Koizumi, K.; Shin, S.; Miyahara, H.; Kimura, A.; Miyamoto, K.; Okuda, T.; Namatame, H.; Taniguchi, M.; Arita, R.; Nagaosa, N.; Kobayashi, K.; Murakami, Y.; Kumai, R.; Kaneko, Y.; Onose, Y.; Tokura, Y. *Nat. Mater.* **2011**, 10, (7), 521-526.
29. Kresse, G.; Joubert, D. *Phys. Rev. B* **1999**, 59, (3), 1758-1775.
30. Perdew, J. P.; Burke, K.; Ernzerhof, M. *Phys. Rev. Lett.* **1996**, 77, (18), 3865-3868.
31. Błoński, P.; Hafner, J. *Phys. Rev. B* **2009**, 79, (22), 224418.
32. Kresse, G.; Furthmüller, J. *Comp. Mater. Sci.* **1996**, 6, (1), 15-50.
33. Bahramy, M. S.; Arita, R.; Nagaosa, N. *Physical Review B* **2011**, 84, (4), 041202.
34. Bawden, L.; Riley, J. M.; Kim, C. H.; Sankar, R.; Monkman, E. J.; Shai, D. E.; Wei, H. I.; Lochocki, E. B.; Wells, J. W.; Meevasana, W.; Kim, T. K.; Hoesch, M.; Ohtsubo, Y.; Le Fèvre, P.; Fennie, C. J.; Shen, K. M.; Chou, F.; King, P. D. C. *Science Advances* **2015**, 1, (8), e1500495.

35. Hsieh, D.; Xia, Y.; Qian, D.; Wray, L.; Dil, J. H.; Meier, F.; Osterwalder, J.; Patthey, L.; Checkelsky, J. G.; Ong, N. P.; Fedorov, A. V.; Lin, H.; Bansil, A.; Grauer, D.; Hor, Y. S.; Cava, R. J.; Hasan, M. Z. *Nature* **2009**, 460, (7259), 1101-1105.
36. Souma, S.; Kosaka, K.; Sato, T.; Komatsu, M.; Takayama, A.; Takahashi, T.; Kriener, M.; Segawa, K.; Ando, Y. *Physical Review Letters* **2011**, 106, (21), 216803.
37. Xu, S.-Y.; Xia, Y.; Wray, L. A.; Jia, S.; Meier, F.; Dil, J. H.; Osterwalder, J.; Slomski, B.; Bansil, A.; Lin, H.; Cava, R. J.; Hasan, M. Z. *Science* **2011**, 332, (6029), 560-564.
38. Neupane, M.; Richardella, A.; Sánchez-Barriga, J.; Xu, S.; Alidoust, N.; Belopolski, I.; Liu, C.; Bian, G.; Zhang, D.; Marchenko, D.; Varykhalov, A.; Rader, O.; Leandersson, M.; Balasubramanian, T.; Chang, T.-R.; Jeng, H.-T.; Basak, S.; Lin, H.; Bansil, A.; Samarth, N.; Hasan, M. Z. *Nat Commun* **2014**, 5, 3841.
39. Liu, Q.; Zhang, X.; Jin, H.; Lam, K.; Im, J.; Freeman, A. J.; Zunger, A. *Physical Review B* **2015**, 91, (23), 235204.
40. Lew Yan Voon, L. C.; Willatzen, M.; Cardona, M.; Christensen, N. E. *Physical Review B* **1996**, 53, (16), 10703-10714.

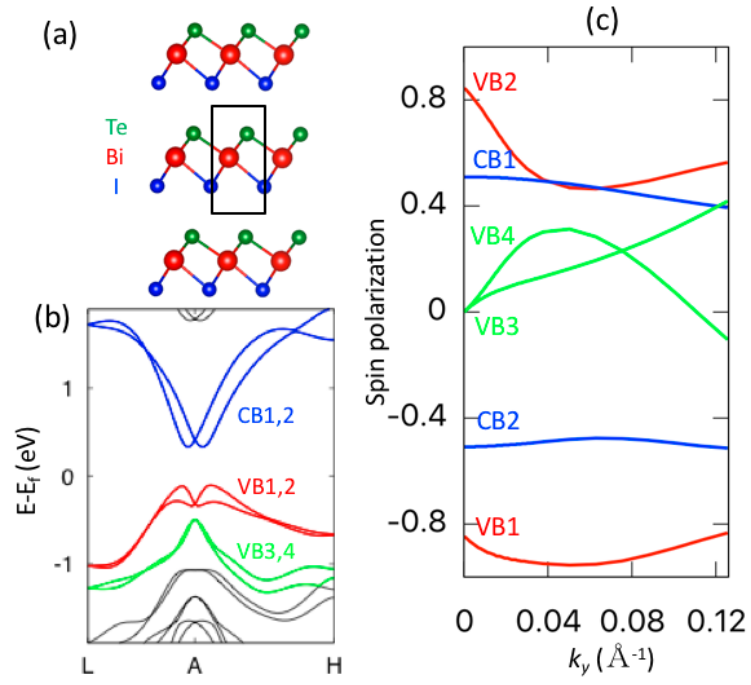


**Fig. 1:** (a) Crystal structure and (b) DFT band structure of BiTeI along the high-symmetric line  $L(0,0.5,0.5) - A(0,0,0.5) - H(1/3,1/3,0.5)$ . (c) Spin polarization  $S_n(\mathbf{k})$  of the six bands VB1-4 and CB1,2 along  $k_y$  direction at the  $k_x = 0$  cut. Note that Spin polarization at  $k_y < 0$  fulfills  $S_1(-\mathbf{k}) = -S_2(\mathbf{k})$  due to Kramer's degeneracy.

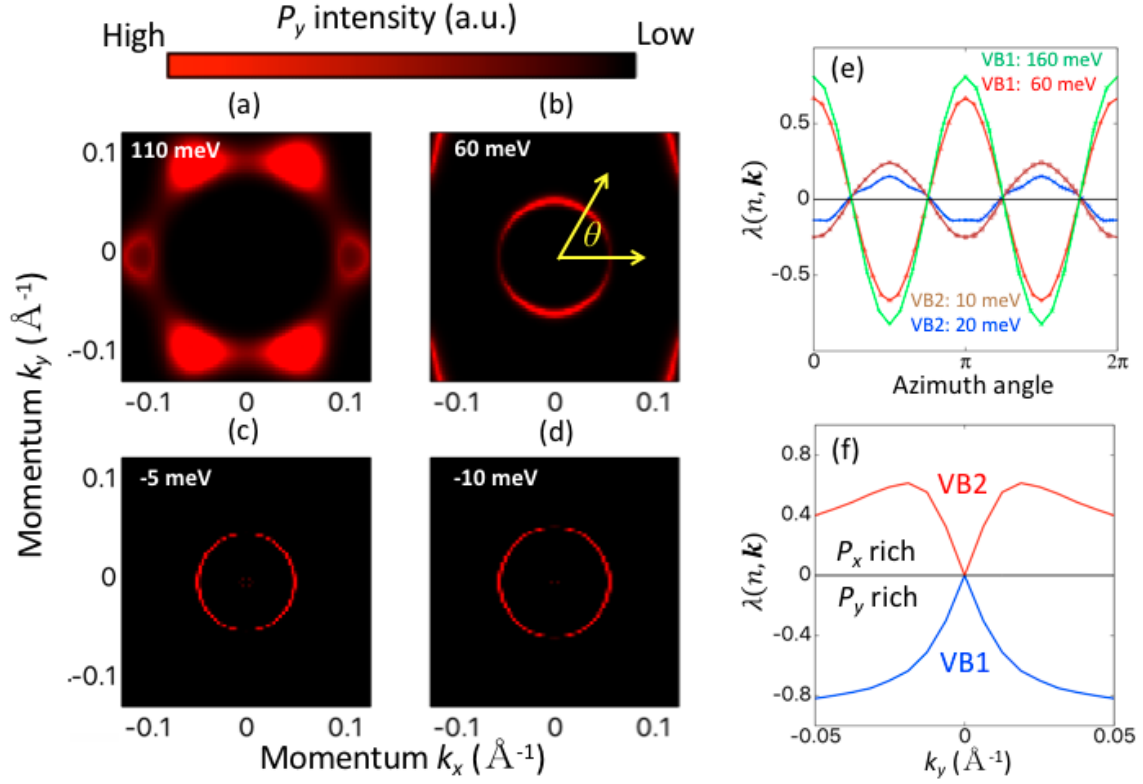


**Fig. 2:** (a-d) Orbital texture indicated by  $p_y$  intensity at different energy contours relative to the band crossing point, (a,b) for VB1 and (c,d) for VB2. (e,f) In-plane orbital polarization  $\lambda$  for (a) different energy contours as a function of the azimuth angle  $\theta$  defined in panel b, and for (f) different spin-splitting bands as a function of the momentum  $k_y$  at the  $k_x = 0$  cut. Note that the orbital polarization switch signs exactly at the band crossing point  $k_y = 0$ .

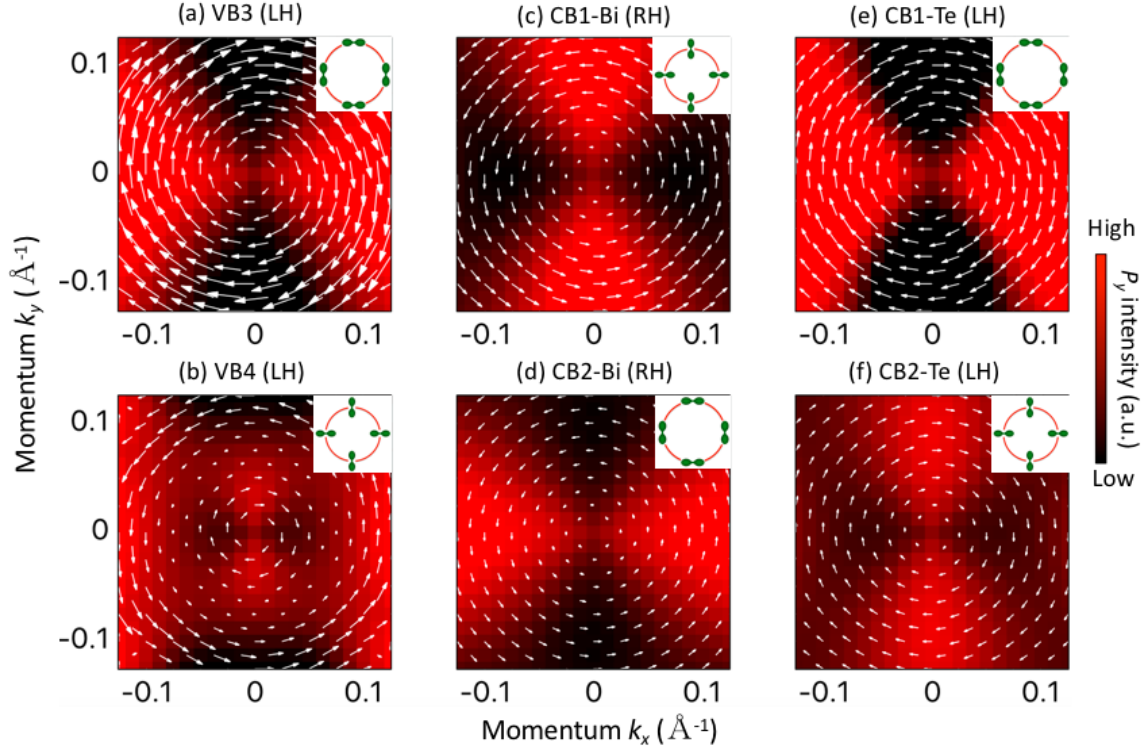


**Fig. 3:** (a,b) The in-plane  $p$ -dependent spin textures (white arrows) and orbital texture (denoted by  $p_y$  orbital intensity as background colors and the inset on the top right) of VB3 (a) and VB4 (b) in the vicinity of the band crossing point. (c,d) The in-plane Bi- $p$ -dependent spin textures and orbital texture of CB1 (c) and CB2 (d) in the vicinity of the band crossing point. (e,f) Same as (c,d) but for Te- $p$ -dependent spin textures of CB1 (e) and CB2 (f).

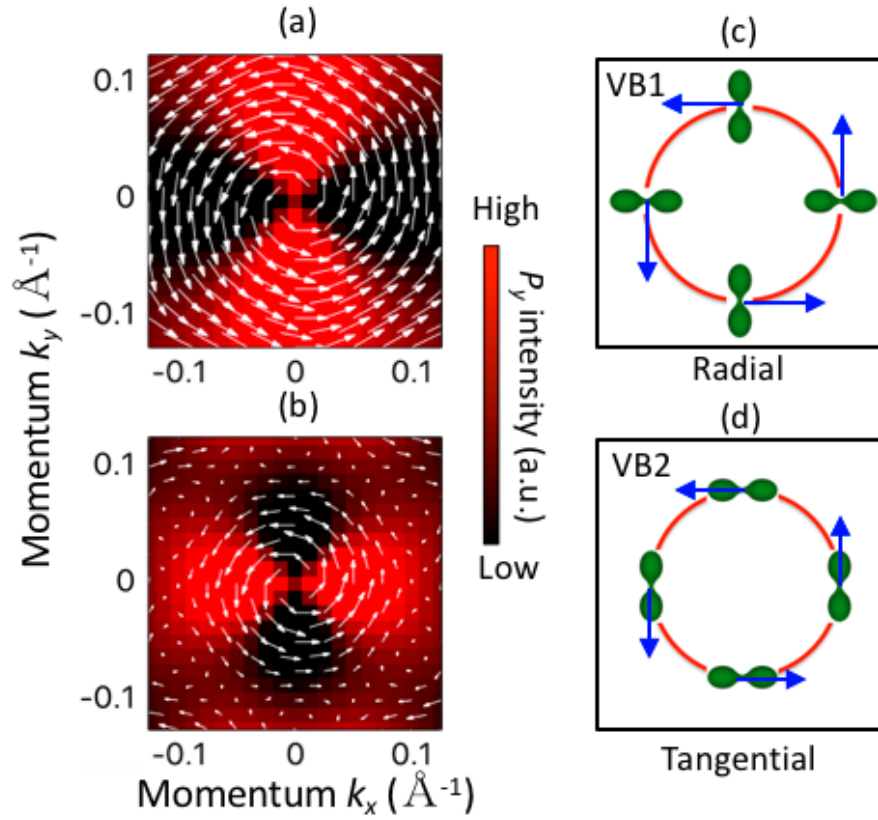


**Fig. 4:** (a,b) The in-plane  $p$ -dependent spin textures (white arrows) for VB1 (a) and VB2 (b). The background color indicates the  $p_y$  intensity. (c,d) Schematic plots for the radial orbital texture and the corresponding orbital-dependent spin texture of VB1 (c) and the tangential orbital texture and the corresponding orbital-dependent spin texture of VB2 (d).

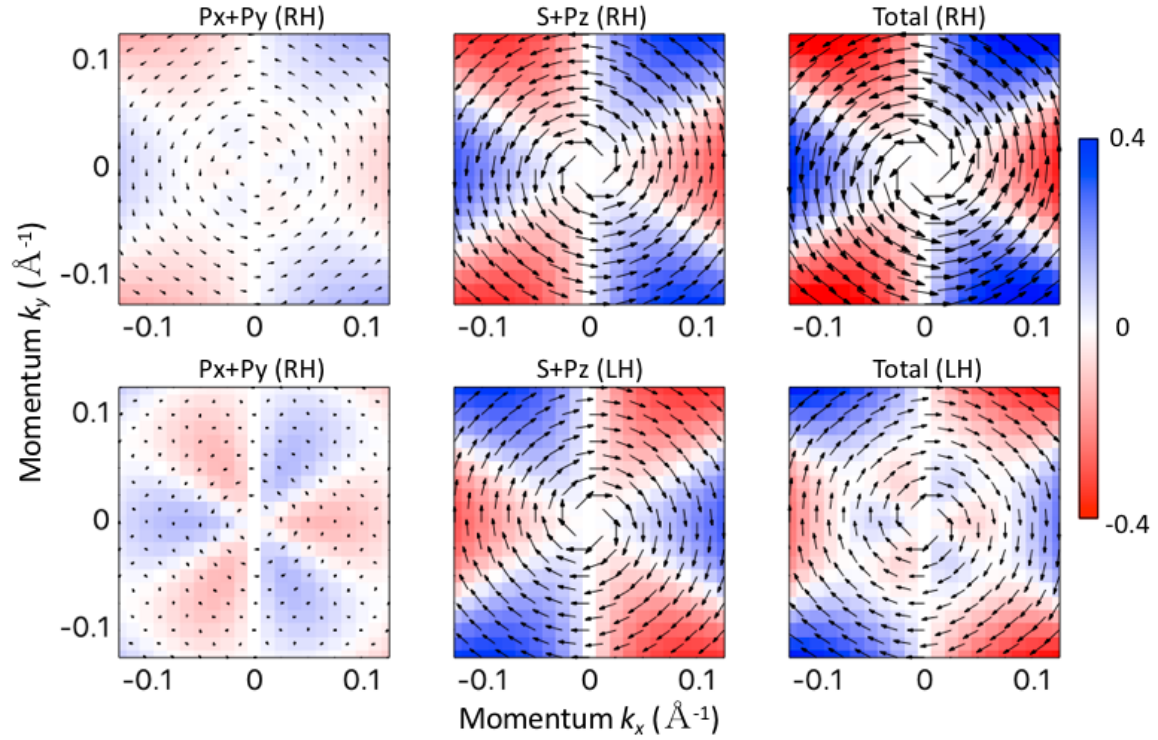


**Fig. 5:** Orbital-dependent spin texture coupled by in-plane  $p$  orbital ( $p_x+p_y$ ) and  $m_l = 0$  orbital ( $s+p_z$ ), and the total spin texture of VB1 (upper row) and VB2 (lower row). The background color indicates the out-of-plane spin component  $S_z$ . LH (RH) denotes left-handed (right-handed) in-plane spin texture ( $S_x, S_y$ ).

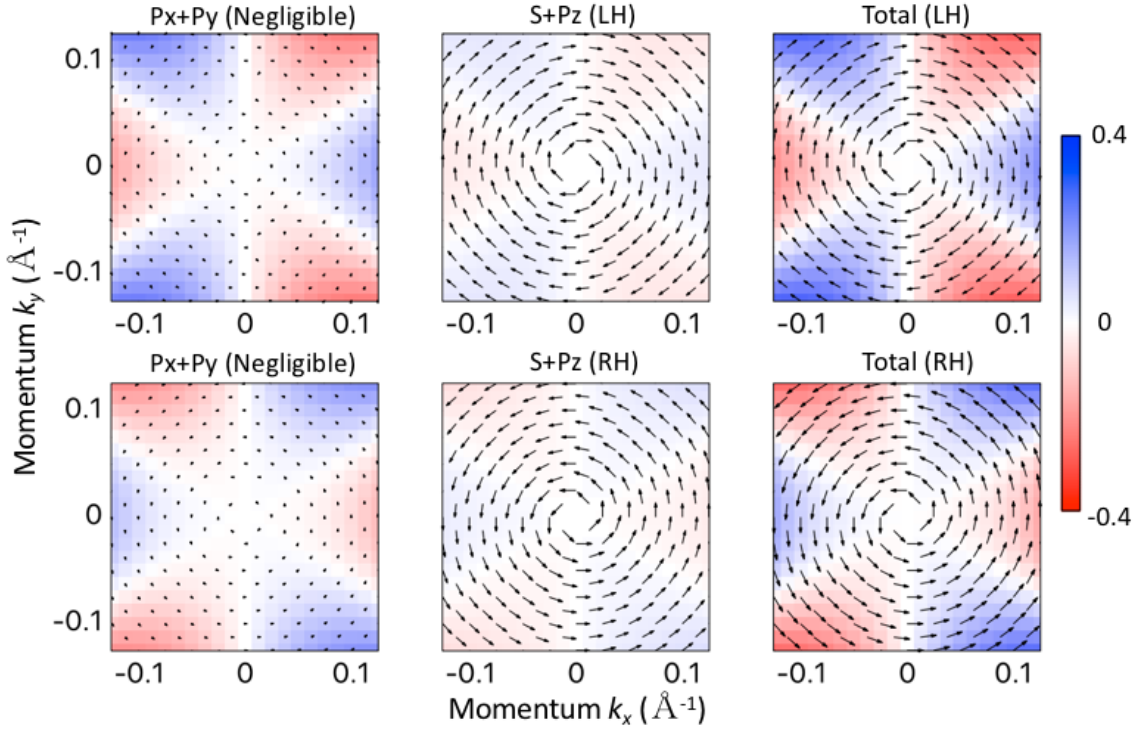


**Fig. 6:** Orbital-dependent spin texture coupled by in-plane  $p$  orbital ( $p_x+p_y$ ) and  $m_l = 0$  orbital ( $s+p_z$ ), and the total spin texture of CB1 (lower row) and CB2 (upper row). The background color indicates the out-of-plane spin component  $S_z$ . LH (RH) denotes left-handed (right-handed) in-plane spin texture ( $S_x, S_y$ ).

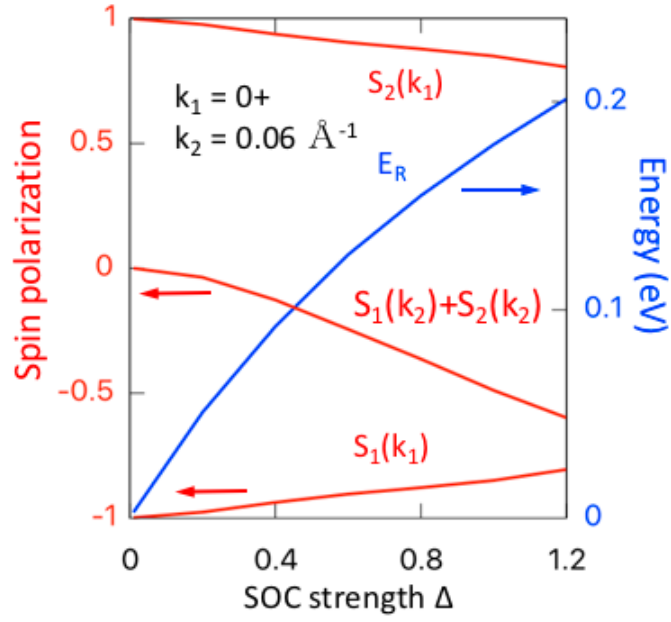


**Fig. 7:** (a) Spin magnitude  $S_1(k_1)$  at  $k_1 = 0+$ ,  $S_1(k_2) + S_2(k_2)$  at  $k_2 = 0.06 \text{ \AA}^{-1}$  along the  $k_y$  direction for VB1 and VB2, and the spin splitting energy  $E_R$  as a function of the strength of SOC.

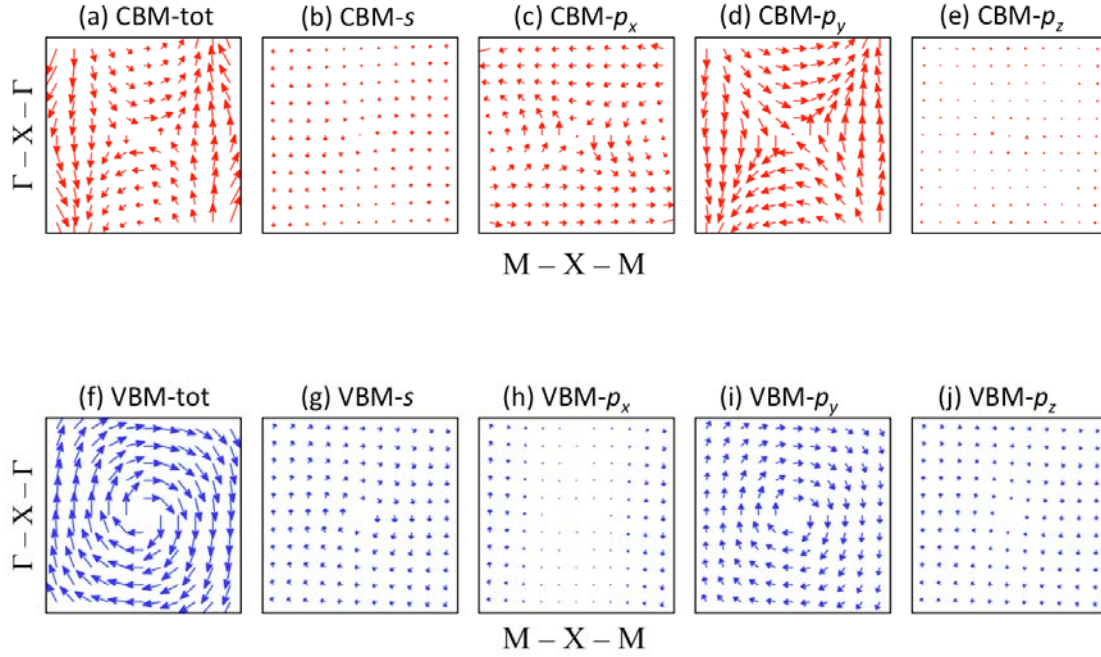


**Fig. 8:** (a) Local spin texture of LaOBiS<sub>2</sub> projected on one BiS<sub>2</sub> layer for CBM. (b-e) Local spin texture for CBM contributed from  $s$ ,  $p_x$ ,  $p_y$  and  $p_z$  atomic orbitals, respectively. (e) Same as (a), but for VBM. (f-j) Same with (b-e), but for VBM. For clarity, the arrow scale of (a-e) is twice as that of (e-h).

Table I: Direction of atomic-orbital dependent spin textures in the vicinity of  $X$  point.  $S_1$  and  $S_2$  form in-plane and perpendicular Bi-S bonds, respectively.

	$s$	$p_x$	$p_y$	$p_z$
Bi	+	+	-	+
$S_1$	-	-	+	-
$S_2$	+	+	-	+

## Appendix. $k \cdot p$ wavefunctions of multi-band Rashba model

The model starts from the basic spin doublets at the band crossing  $K^*$  point and expands the wavefunctions to a small wave vector  $\mathbf{k}$  away from  $K^*$  [Eq. (3) and (4) of the main text], to see how different  $p$  orbitals couple the spin angular momentum with a LH or RH texture. Without the loss of generality, we consider the  $K^*$  state with the azimuth total angular momentum  $m_j$  being  $\pm 1/2$ , as the case of VB1 and VB2 in BiTeI (double group representation  $A_4$ ). We can therefore write the doubly degenerate states at the A point as<sup>33, 40</sup>:

$$|A_{4v}, \frac{1}{2}\rangle = \sqrt{1 - \omega_{VB}^2} |+\rangle \otimes |\downarrow\rangle + \omega_{VB} |Z\rangle \otimes |\uparrow\rangle \quad (\text{A1})$$

$$|A_{4v}, -\frac{1}{2}\rangle = \sqrt{1 - \omega_{VB}^2} |-\rangle \otimes |\uparrow\rangle + \omega_{VB} |Z\rangle \otimes |\downarrow\rangle \quad (\text{A2})$$

where  $\omega_{VB}$  is the wavefunction coefficient that can be determined by DFT calculation.  $|Z\rangle = \omega_s |s\rangle + \omega_z |p_z\rangle$  with  $|\omega_s|^2 + |\omega_z|^2 = 1$  and  $|\pm\rangle = \mp(|p_x\rangle \pm i|p_y\rangle)/\sqrt{2}$  stand for different orbital basis. The  $|+\rangle$ ,  $|-\rangle$  and  $|Z\rangle$  basis hold the orbital angular momentum  $m_l = 1, -1$ , and  $0$ , respectively, coupling with certain spin angular momenta to preserve the total angular momentum  $m_j$ . Although the spin splitting happens at the wavevectors away from A, the zero-order wave functions at A still need to approximately fit the Rashba Hamiltonian  $H_R = \alpha(\sigma_y k_x - \sigma_x k_y)$ , written as the matrix form in the following:

$$H_R = \alpha |k| \begin{pmatrix} 0 & -ie^{-i\theta} \\ ie^{i\theta} & 0 \end{pmatrix} \quad (\text{A3})$$

Therefore, the zero-order wavefunctions at A are written as:

$$\begin{aligned} |\text{VB1}, 0+\rangle &= \frac{1}{\sqrt{2}} \left[ -ie^{-i\theta} |A_{4v}, \frac{1}{2}\rangle + |A_{4v}, -\frac{1}{2}\rangle \right] = \\ & \frac{1}{\sqrt{2}} \left[ \sqrt{1 - \omega_{VB}^2} |-\rangle - ie^{-i\theta} \omega_{VB} |Z\rangle \right] \otimes |\uparrow\rangle - \left[ \frac{1}{\sqrt{2}} ie^{-i\theta} \sqrt{1 - \omega_{VB}^2} |+\rangle - \omega_{VB} |Z\rangle \right] \otimes |\downarrow\rangle \quad (\text{A4}) \end{aligned}$$

$$\begin{aligned} |\text{VB1}, 0-\rangle &= \frac{1}{\sqrt{2}} \left[ ie^{-i\theta} |A_{4v}, \frac{1}{2}\rangle + |A_{4v}, -\frac{1}{2}\rangle \right] = \\ & \frac{1}{\sqrt{2}} \left[ \sqrt{1 - \omega_{VB}^2} |-\rangle + ie^{-i\theta} \omega_{VB} |Z\rangle \right] \otimes |\uparrow\rangle + \left[ \frac{1}{\sqrt{2}} ie^{-i\theta} \sqrt{1 - \omega_{VB}^2} |+\rangle + \omega_{VB} |Z\rangle \right] \otimes |\downarrow\rangle \quad (\text{A5}) \end{aligned}$$

Using the rotational in-plane coordinate system with tangential, radial direction to present the quantum number states  $|+\rangle$  and  $|-\rangle$ , we have

$$\begin{pmatrix} |+\rangle \\ |-\rangle \end{pmatrix} = \frac{1}{\sqrt{2}} \begin{pmatrix} -1 & -i \\ 1 & -i \end{pmatrix} \begin{pmatrix} |p_x\rangle \\ |p_y\rangle \end{pmatrix} = \frac{1}{\sqrt{2}} \begin{pmatrix} -ie^{i\theta} & -e^{i\theta} \\ -ie^{-i\theta} & e^{-i\theta} \end{pmatrix} \begin{pmatrix} p_t \\ p_r \end{pmatrix} \quad (\text{A6})$$

For the spin part, we use  $|LH\rangle$  and  $|RH\rangle$  helical spin state to present  $|\uparrow\rangle$  and  $|\downarrow\rangle$ :

$$\begin{pmatrix} |\uparrow\rangle \\ |\downarrow\rangle \end{pmatrix} = \frac{1}{\sqrt{2}} \begin{pmatrix} -ie^{i\theta} & ie^{i\theta} \\ 1 & 1 \end{pmatrix} \begin{pmatrix} |LH\rangle \\ |RH\rangle \end{pmatrix} \quad (\text{A7})$$

Then we can rewrite Eq. (S6) and (S7) as:

$$|VB1,0+\rangle = \frac{1}{\sqrt{2}} \sqrt{1 - \omega_{VB}^2} |p_t\rangle \otimes |LH\rangle + [-\frac{i}{\sqrt{2}} \sqrt{1 - \omega_{VB}^2} |p_r\rangle + \omega_{VB} |Z\rangle] \otimes |RH\rangle \quad (\text{A8})$$

$$|VB2,0+\rangle = -\frac{1}{\sqrt{2}} \sqrt{1 - \omega_{VB}^2} |p_t\rangle \otimes |RH\rangle + [\frac{i}{\sqrt{2}} \sqrt{1 - \omega_{VB}^2} |p_r\rangle + \omega_{VB} |Z\rangle] \otimes |LH\rangle \quad (\text{A9})$$

These are the zero-order wavefunctions of A states with the azimuth total angular momentum  $m_j = 1/2$ . Eq. (A8) and (A9) already reveal many observations found by our DFT calculation in the main text. For example, the tangential orbital always couples opposite spin textures with the radial orbital and  $s$  and  $p_z$  orbitals. Furthermore, at A point the tangential and radial orbitals have the same intensity but opposite spin textures cancelling each other. Therefore, the spin magnitude at A point is determined by the intensity of  $s$  and  $p_z$  orbitals.

The first-order wavefunctions at A point involve linear  $k$  term, which can be presented using  $k_{\pm}$  that have fixed  $m_l = \pm 1$ , written as

$$|A_{4v}, \frac{1}{2}\rangle^{(1)} = a_{VB} k_+ |Z\rangle \otimes |\downarrow\rangle + b_{VB} k_+ |-\rangle \otimes |\uparrow\rangle + c_{VB} k_- |+\rangle \otimes |\uparrow\rangle \quad (\text{A10})$$

$$|A_{4v}, -\frac{1}{2}\rangle^{(1)} = -a_{VB} k_- |Z\rangle \otimes |\uparrow\rangle - b_{VB} k_- |+\rangle \otimes |\downarrow\rangle - c_{VB} k_+ |-\rangle \otimes |\downarrow\rangle \quad (\text{A11})$$

where  $k_{\pm} = k_x \pm ik_y$ , and  $a_{VB}$ ,  $b_{VB}$ ,  $c_{VB}$  are wavefunction coefficients. Note that we have used the conservation of the total angular momentum along the  $z$  direction to construct the wavefunctions by involving the angular momentum of  $k_{\pm}$  as  $\pm 1$ , while  $|+\rangle \otimes |\uparrow\rangle$  and  $|-\rangle \otimes |\downarrow\rangle$  themselves are ‘‘heavy hole’’ like components with  $m_j = \pm 3/2$ . Similarly,

considering the Rashba Hamiltonian the first-order wavefunctions of the valence bands are written as

$$|\text{VB1}, k\rangle^{(1)} = \frac{1}{\sqrt{2}} \left[ -ie^{-i\theta} |A_{4v}, \frac{1}{2}\rangle + |A_{4v}, -\frac{1}{2}\rangle \right] =$$

$$\frac{i}{\sqrt{2}} (b_{VB} + c_{VB}) k |p_t\rangle \otimes |LH\rangle + \left[ \frac{1}{\sqrt{2}} (b_{VB} - c_{VB}) k |p_r\rangle - ia_{VB} k |Z\rangle \right] \otimes |RH\rangle \quad (\text{A12})$$

$$|\text{VB2}, k\rangle^{(1)} = \frac{1}{\sqrt{2}} \left[ ie^{-i\theta} |A_{4v}, \frac{1}{2}\rangle + |A_{4v}, -\frac{1}{2}\rangle \right] =$$

$$\frac{i}{\sqrt{2}} (b_{VB} + c_{VB}) k |p_t\rangle \otimes |RH\rangle + \left[ \frac{1}{\sqrt{2}} (b_{VB} - c_{VB}) k |p_r\rangle + ia_{VB} k |Z\rangle \right] \otimes |LH\rangle \quad (\text{A13})$$

Considering  $\mu_{VB} = i(b_{VB} + c_{VB})$ ,  $v_{VB} = b_{VB} - c_{VB}$  and  $\xi_{VB} = ia_{VB}$  and combining zero-order and first-order wavefunctions Eq. (A8), (A9), (A12) and (A13) together we obtain the exact form of Eq. (3) and (4). In addition, only if  $c_{VB} = 0$ , i.e., the  $|+\rangle \otimes |\uparrow\rangle$  and  $|-\rangle \otimes |\downarrow\rangle$  components in Eq. (A10) and (A11) are absent, would avoid the orbital switching. Therefore, the origin of the orbital texture switch is attributed to the mixing of  $m_j = \pm 3/2$  states.